The Astrophysical Journal Letters, 823:L5 (7pp), 2016 May 20 doi:10.3847/2041-8205/823/1/L5

AN ANALYSIS OF INTERPLANETARY SOLAR RADIO EMISSIONS ASSOCIATED WITH A CORONAL MASS EJECTION

V. Krupar[1,2], J. P. Eastwood[1], O. Kruparova[2], O. Santolik[2,3], J. Soucek[2], J. Magdalenić[4], A. Vourlidas[5], M. Maksimovic[6], X. Bonnin[6], V. Bothmer[7], N. Mrotzek[7], A. Pluta[7], D. Barnes[8], J. A. Davies[8], J. C. Martínez Oliveros[9], and S. D. Bale[9,10]
[1] The Blackett Laboratory, Imperial College London, London, UK; v.krupar@imperial.ac.uk, jonathan.eastwood@imperial.ac.uk
[2] Institute of Atmospheric Physics CAS, Prague, Czech Republic; ok@ufa.cas.cz, os@ufa.cas.cz, soucek@ufa.cas.cz
[3] Faculty of Mathematics and Physics, Charles University, Prague, Czech Republic
[4] Solar-Terrestrial Center of Excellence-SIDC, Royal Observatory of Belgium, Brussels, Belgium; jasmina.magdalenic@oma.be
[5] The Johns Hopkins University Applied Physics Laboratory, Laurel, MD, USA; angelos.vourlidas@jhuapl.edu
[6] LESIA, UMR CNRS 8109, Observatoire de Paris, Meudon, F-92195 France; milan.maksimovic@obspm.fr, xavier.bonnin@obspm.fr
[7] Institut für Astrophysik, Göttingen University, Göttingen, Germany; bothmer@astro.physik.uni-goettingen.de, nmrotzek@astro.physik.uni-goettingen.de, apluta@astro.physik.uni-goettingen.de
[8] RAL Space, Rutherford Appleton Laboratory, Harwell Campus, Oxford, UK; david.barnes@stfc.ac.uk, jackie.davies@stfc.ac.uk
[9] Space Sciences Laboratory, University of California, Berkeley, CA, USA; oliveros@ssl.berkeley.edu, bale@ssl.berkeley.edu
[10] Physics Department, University of California, Berkeley, CA, USA
Received 2016 March 21; revised 2016 April 29; accepted 2016 April 29; published 2016 May 12

ABSTRACT

Coronal mass ejections (CMEs) are large-scale eruptions of magnetized plasma that may cause severe geomagnetic storms if Earth directed. Here, we report a rare instance with comprehensive in situ and remote sensing observations of a CME combining white-light, radio, and plasma measurements from four different vantage points. For the first time, we have successfully applied a radio direction-finding technique to an interplanetary type II burst detected by two identical widely separated radio receivers. The derived locations of the type II and type III bursts are in general agreement with the white-light CME reconstruction. We find that the radio emission arises from the flanks of the CME and are most likely associated with the CME-driven shock. Our work demonstrates the complementarity between radio triangulation and 3D reconstruction techniques for space weather applications.

Key words: solar–terrestrial relations – Sun: coronal mass ejections (CMEs) – Sun: radio radiation

1. INTRODUCTION

Type II and type III bursts are generally associated with solar eruptive events (Wild 1950; Wild & McCready 1950; Ginzburg & Zhelezniakov 1958; Melrose 1980). Both are generated, via the plasma emission mechanism, when beams of suprathermal electrons interact with ambient plasma generating radio emissions at the plasma frequency f_p (the fundamental emission) or its second harmonic $2f_p$ (the harmonic emission). As the electron beams propagate outward from the Sun, radio emissions are generated at progressively lower frequencies corresponding to a decreasing ambient density. Type II bursts are generated by electron beams accelerated at the shock fronts ahead of propagating coronal mass ejections (CMEs), while type III bursts are a consequence of impulsively accelerated electrons associated with solar flares (e.g., Reiner et al. 1998a, 2001; Gopalswamy et al. 2000; Cairns et al. 2003; Cremades et al. 2007; Krupar et al. 2015). Although type II bursts generated in the solar corona are routinely measured from the ground, spacecraft observations of type II bursts originating further from the Sun, in the interplanetary medium—especially with a good signal-to-noise ratio—are relatively rare (Reiner et al. 1998b; Vourlidas 2004; Gopalswamy et al. 2005). Moreover, interplanetary type II bursts are usually patchy and intermittent with short periods of radio enhancements (Kaiser et al. 1998; Reiner et al. 2003). It has been suggested that these enhancements are related to CME–CME or CME–streamer interactions (Gopalswamy et al. 2001; Xie et al. 2012).

Over the past decade, we have benefited from multipoint radio measurements obtained by the twin-spacecraft *Solar TErrestrial RElations Observatory* (*STEREO*) mission (Bale et al. 2008; Bougeret et al. 2008), launched in 2006, which allow us to localize radio sources in the interplanetary medium between 2.5 kHz and 16 MHz (e.g., Reiner et al. 2009; Thejappa & MacDowall 2010; Martínez Oliveros et al. 2012a; Martínez-Oliveros et al. 2015). Using direction-finding radio data recorded by the *STEREO-B* and *Wind* spacecraft, Martínez Oliveros et al. (2012b) present an analysis of an interplanetary type II burst associated with a CME–CME interaction. More recently, Magdalenić et al. (2014) performed a direction-finding analysis of another event using the same pair of spacecraft suggesting that an interplanetary type II burst was, in this case, related to a CME–streamer interaction.

Here, we use data obtained by the *STEREO*/Waves/High Frequency Receiver (125 kHz–2 MHz), which allows us to localize radio sources with distances from 5 solar radii ($1\,R_S = 695{,}500$ km) above the Sun's surface up to 1 astronomical unit (1 au = 149,598,000 km; Cecconi et al. 2008; Krupar et al. 2010, 2012). We also analyze data from the *STEREO*/Sun Earth Connection Coronal and Heliospheric Investigation (SECCHI; Howard et al. 2008) package, the *MErcury Surface, Space ENvironment, GEochemistry, and Ranging* (*MESSENGER*) spacecraft and by the *Solar Heliospheric Observatory* (*SOHO*; Domingo et al. 1995; Solomon et al. 2007).

In this Letter, we present a study of CME kinematics using white-light, radio, and plasma measurements obtained by the *STEREO*, *SOHO*, and *MESSENGER* spacecraft. We demonstrate that interplanetary solar radio emissions can be used for estimating both CME speeds and directions.

2. OBSERVATIONS AND ANALYSIS

The CME of particular interest first appeared in the field of view of the *SOHO*/LASCO C2 coronagraph at 17:24 UT on 2013 November 29. At the time of the event, the *STEREO-A*

and *STEREO-B* spacecraft were 150° of heliocentric Earth equatorial (HEEQ) longitude ahead of and 147° behind the Earth, at heliocentric distances of 0.96 au and 1.08 au, respectively. *SOHO* was at the first Sun–Earth Lagrangian point (L_1), located some 1.5 million km upstream of the Earth. *MESSENGER* was at an HEEQ longitude of 132° and a heliocentric distance of 0.40 au.

2.1. White-light Observations

This favorable configuration of *SOHO* and *STEREO* allows us to apply the graduated cylindrical shell (GCS; Thernisien et al. 2009) model to coronagraph images simultaneously recorded by these three spacecraft in order to reconstruct the CME leading edge in three dimensions (3D). We performed this analysis using images taken between 20:00 UT and 23:30 UT on November 29, when the CME was well observed by all three spacecraft (Figure 1). From GCS fitting, we estimate the radial distance of the leading edge r_{GCS}, leading to a calculated average CME speed of 761 ± 13 km s^{-1} with a launch time of 19:42 UT. The CME angular half-width λ_{GCS} was estimated to be 59°. The HEEQ longitude of propagation of the CME from GCS fitting was 128°, which is roughly toward *MESSENGER*. To calculate the speed further out in the heliosphere, we also applied the self-similar expansion fitting (SSEF) technique to *STEREO-A*/HI data (Davies et al. 2012, Equation (6)). Using λ_{GCS} as input, SSEF yielded a CME radial speed of 862 ± 8 km s^{-1}, liftoff at 19:17 UT, and an HEEQ propagation longitude of 135°. These values are in very good agreement with those from the GCS fit. However, note that the GCS and SSEF predicted liftoff times are two hours later than when the CME was first seen by *SOHO*, as the CME accelerated considerably near the Sun's surface (Gopalswamy et al. 2015). Inspection of the EUVI images shows that the liftoff time is about 16:00 UT and the onset can be characterized as streamer blowout CME.

2.2. Radio Emission

This CME was accompanied by interplanetary type II and type III bursts detected by both *STEREO* spacecraft on 2013 November 29–30 (Figure 2). Since the CME was launched from the far side of the Sun, ground-based high-frequency radio measurements of the associated radio bursts are absent. Figures 2(a) and (b) display the radio flux density S measured by *STEREO-A* and *STEREO-B*, respectively. The type III burst at 22:00 UT on November 29 is followed by the intermittent type II burst, over an interval of seven hours. Within this, we were able to identify three intervals when the signal at both spacecraft was intense enough to enable successful direction-finding analysis: at 22:30 UT (1500 kHz) on November 29 and at 00:30 UT (600 kHz) and 04:00 UT (300 kHz) on the next day.

A recent Schmidt & Cairns (2016) data-driven MHD simulation of this event with an analytic quantitative kinetic model for the radio emission concludes that the type II burst intervals of interest here are the fundamental emission. To compare radio measurements with the CME propagation parameters, we converted the radial distances yielded by the GCS fit r_{GCS} to frequencies f using the density model of Sittler & Guhathakurta (1999) assuming the fundamental emission. We consider the type II burst to be generated at both the CME leading edge ($f \sim r_{GCS}$) and flanks ($f \sim r_{GCS} \cos \lambda_{GCS}$). The type II burst coincides well with the kinematic curve that corresponds to CME flanks (Figure 2(c)). Although type II bursts are generated at interplanetary shock fronts of propagating CMEs, they predominantly appear close to CME flanks (e.g., Gary et al. 1984; Magdalenić et al. 2014). For our wave propagation analysis, we applied the singular value decomposition technique to multicomponent measurements of auto- and cross-correlations of the voltages induced by electric field fluctuations (Santolík et al. 2003; Krupar et al. 2012). Figures 2(c)–(f) present the calculated wave vector directions θ and ϕ in the radial-tangential-normal (RTN) coordinate system (a spacecraft centered coordinate system where the Sun is at ($\theta = 90°$, $\phi = 0°$), southward/northward is ($\theta = 0°$, 180°), and east/west is ($\pm\phi = 90°$). An intensity threshold ($S > 5 \times 10^{-19}$ W m^{-2} Hz^{-1}) has been applied to suppress the background. The high-frequency portions of the type II and type III bursts (∼>1 MHz) propagate roughly toward *STEREO-A*, whereas the low-frequency portions propagate east of the spacecraft (Figure 2(e)). For *STEREO-B*, the type II and type III bursts propagate east of the spacecraft for over the entire interval analyzed (Figure 2(f)).

At this time, the separation angle between the two *STEREO* spacecraft was 64°, which allows us to accurately locate the sources of the type II and type III bursts by triangulation (Krupar et al. 2014a, 2014b). We note that this favorable separation angle would be also attained for combined spacecraft observations from L_1 and the fifth Sun–Earth Lagrangian point (L_5; Gopalswamy et al. 2011a, 2011b; Vourlidas 2015). Data points around the maximum flux densities of the type II and type III bursts were carefully selected in order to perform the radio triangulation. The triangulated type II and type III radio bursts are clustered along the CME propagation direction that is predicted by the GCS and SSEF fits, with radial distances ranging from 0.12 to 0.31 au (Figure 3). We find that, for this interval, the radio sources are located considerably further from the Sun when compared to the density model of Sittler & Guhathakurta (1999), which predicts radial distances between 0.03 au (1500 kHz) and 0.10 au (300 kHz). This ambiguity is probably caused by radio sources being spatially extended and/or radio propagation effects (Steinberg et al. 1984, 1985; Thejappa et al. 2007; Krupar et al. 2014a). Averaged radio locations of the three analyzed intervals of the type II burst are as follows: 0.23 ± 0.02 au (22:30 UT), 0.21 ± 0.03 au (00:30 UT), and 0.32 ± 0.04 UT (04:00 UT). The source locations derived from the triangulation of the second interval are systematically located closer to the Sun than those of the first one, when it would be expected to be further from the Sun. This discrepancy is probably caused by the superposition of the signal of the second interval of the type II burst with a fast-drifting emission occurring at about the same time. We thus will not include triangulated radio locations of the second interval in our analysis. The calculated average speed of the CME-driven shock based on the triangulated source locations of the first and third interval is 656 km s^{-1}, which is lower than those predicted by the GCS and SSEF fits. The third interval was also observed by the *Wind*/Waves instrument at 332 kHz located at the L_1 point (Bougeret et al. 1995). It yielded a wave vector azimuth $\phi_{RTN} = -12°$, which is a good agreement with the triangulated location by *STEREO*/Waves, which would be observed at $\phi_{RTN} = -9°$ by *Wind*/Waves.

We have examined *STEREO-A*/SECCHI/COR2 images in order to compare the relative positions of the triangulated

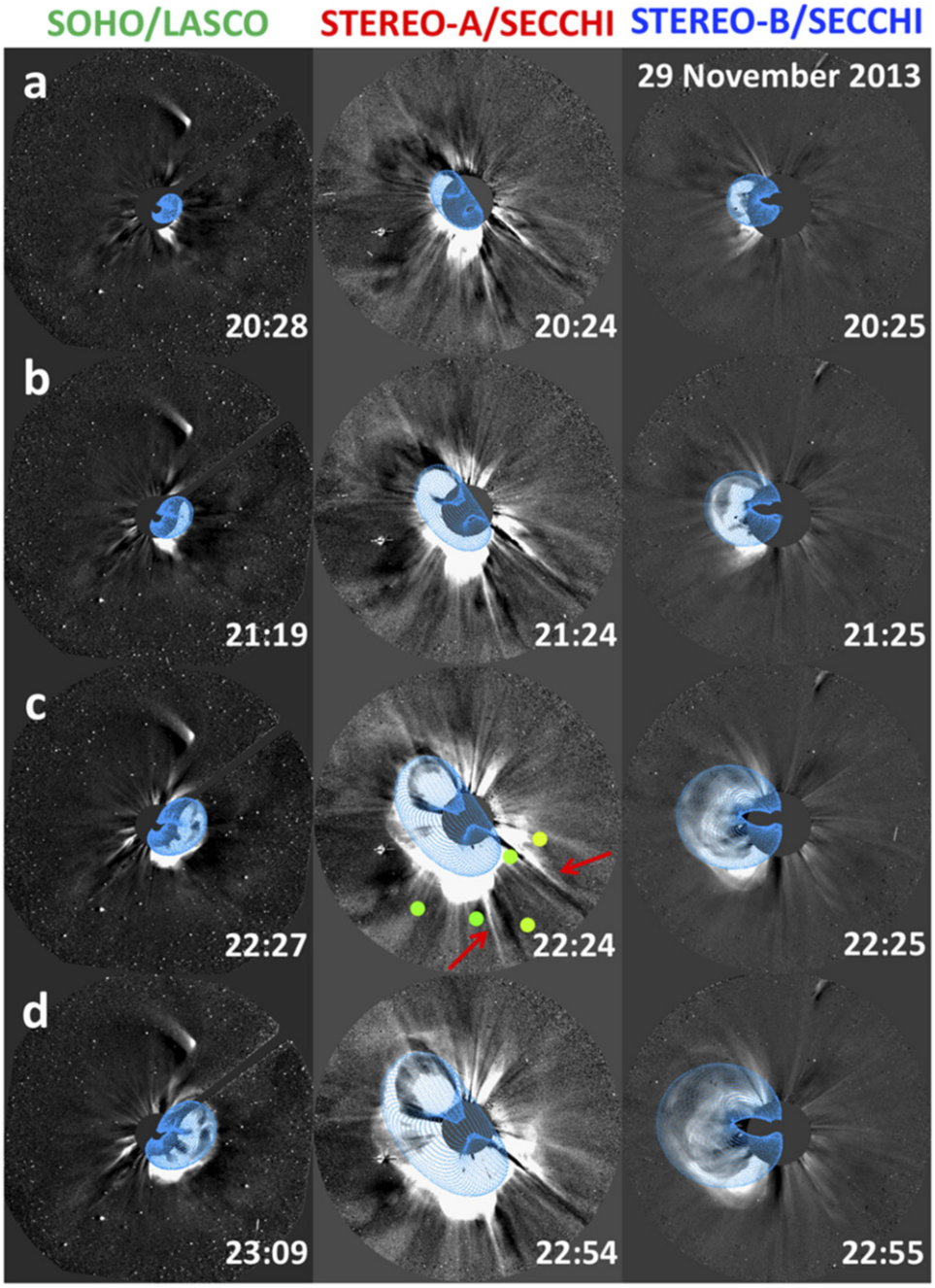

Figure 1. White-light observations of the CME on 2013 November 29 by the *SOHO*/LASCO/C3 and *STEREO*/SECCHI/COR2 instruments. (a)–(d) Fit of the GCS model (blue grid) overlaid on multipoint coronagraph observations, from left to right: *SOHO*, *STEREO*-A, and *STEREO*-B. Radio locations of the type II burst observed on November 29 are denoted by green circles in (c). Used colors correspond to those in Figure 3.

source locations of the first interval of the type II burst with coronal structures (Figure 1(c)). The type II burst sources are clustered along positions of two streamers located at the west limb and at the southern CME flank (see the red arrows in Figure 1(c)). This suggests a close relationship between the type II burst and a possible interaction between the CME-driven shock and these streamers. It is consistent with the work of Magdalenić et al. (2014), who reported a similar result for a different CME. We note that another CME is already in progress along the south and appears to overlap with the radio sources. Inspection of the EUVI images shows that the CME is associated with a slow filament eruption starting earlier on the same day and appears to propagate at a plane about 90° away from the source of our CME. Therefore, it is unlikely that it is affecting our observations or interpretation.

2.3. In Situ Measurements

Figure 4 shows measurements obtained by *MESSENGER* and *STEREO-A*. A fast forward interplanetary shock was observed by *MESSENGER*, at 0.4 au, at around 14:30 UT on November 30 (Figure 4(a)), identified by a sharp increase in the magnetic field magnitude (from 10 to 55 nT). This shock was likely to have been driven by the CME analyzed in this study. From the CME launch time and the arrival time of the shock at *MESSENGER*, we estimate the average CME speed between

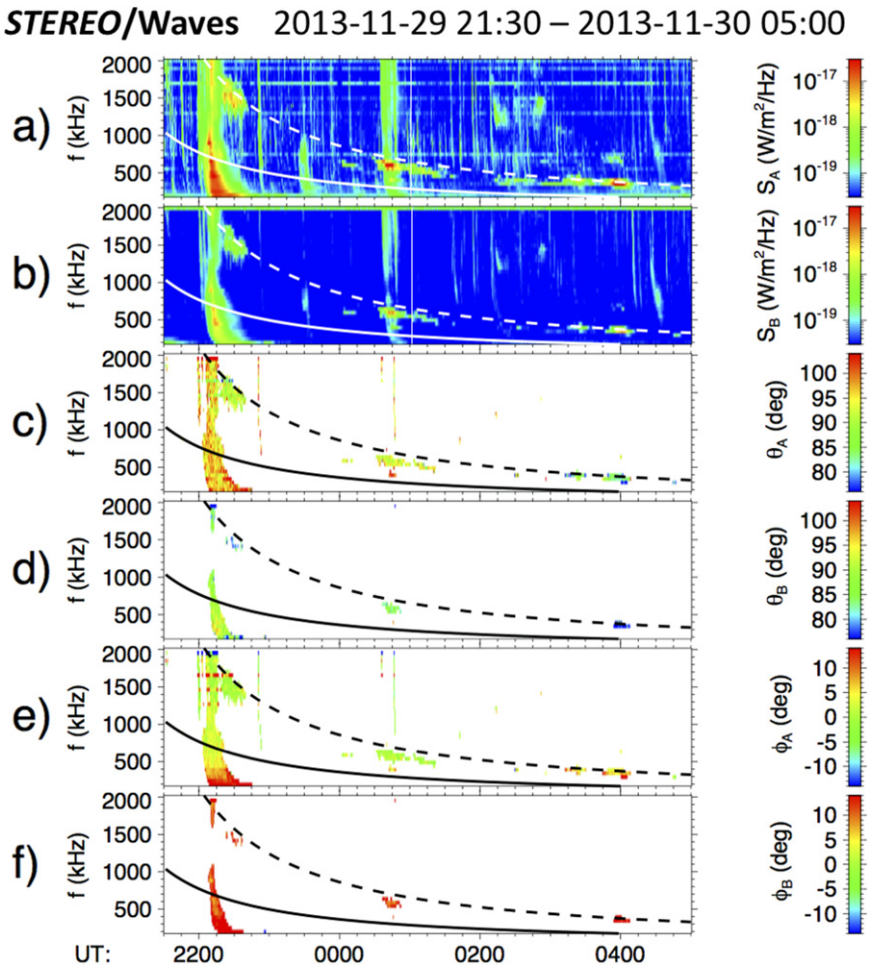

Figure 2. Radio measurements of type II and type III bursts. (a), (b) Radio flux density S. (c), (d) Colatitude of wave vector θ. (e), (f) Azimuth of wave vector ϕ. Solid and dashed lines denote results of the GCS model assuming emission at the leading edge and flanks, respectively.

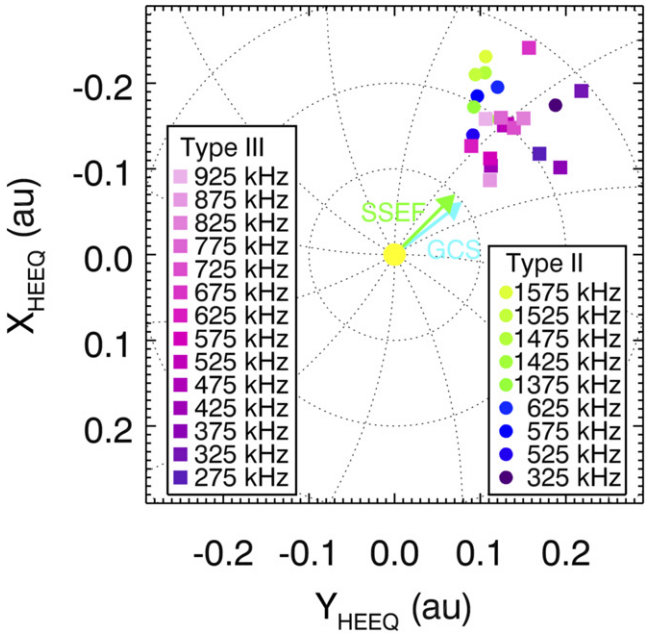

Figure 3. Propagation analysis of radio measurements. Radio source locations of type II (circles) and type III (squares) bursts for four time-frequency intervals in the XY_{HEEQ} plane. Colors denote frequencies. The cyan and green arrows indicate the CME propagation directions obtained by the GCS model and the SSEF technique, respectively. The Sun is at (0, 0).

the Sun and *MESSENGER* to be $\sim$741 km s^{-1}. The CME-driven shock was also detected in situ at *STEREO-A*, at 0.96 au, at around 22:30 UT on December 1 (Figures 4(b)–(d)). Shock arrival corresponds to an abrupt increases in the magnetic field (from 7 to 20 nT), proton density (1 to 12 cm^{-3}), and proton bulk velocity (340 to 580 km s^{-1}). From the CME launch time and the time of shock arrival at *STEREO-A*, we estimated the average CME speed to be 734 km s^{-1}. From the times of shock arrival at *MESSENGER* and *STEREO-A*, we estimate a CME speed between the two spacecraft of 729 km s^{-1}. The shock speed calculated by assuming the shock mass flux conservation equation over the shock, measured by *STEREO-A*, is 602 km s^{-1}. Figure 4(e) presents radio and plasma waves measurements recorded by the low-frequency receiver on board *STEREO-A* (2.5–160 kHz). We observe large amplitude Langmuir waves and a harmonic emission of a slow drifting type II burst in upstream of the CME-driven shock. We note that it is the first observation of the source region of an interplanetary type II burst by *STEREO* (Graham & Cairns 2015).

2.4. Kinematics of the CME and CME-driven Shock

Figure 5 shows an overview of the results obtained for the CME and CME-driven shock propagation. We have averaged azimuths ϕ of the type II and type III burst source locations

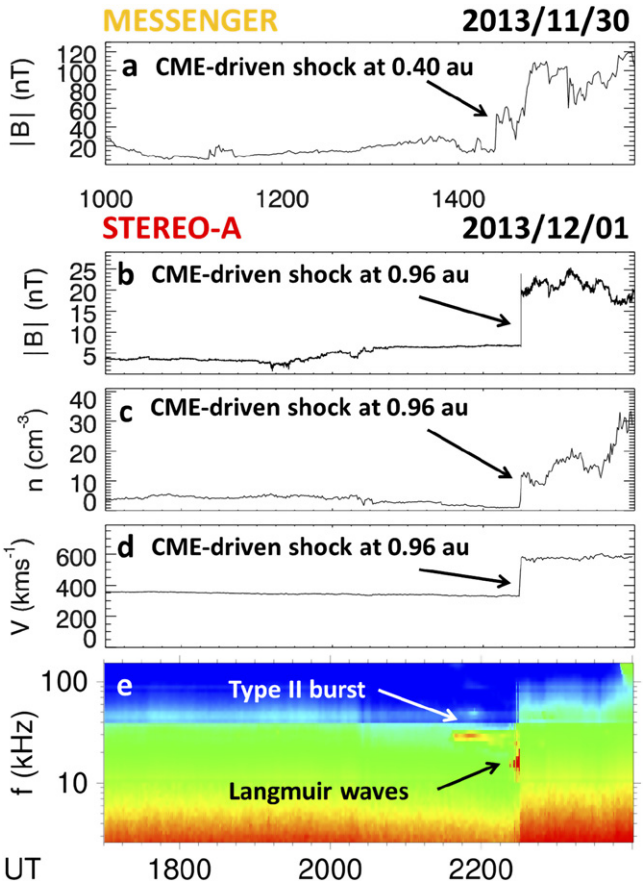

Figure 4. Observations of the CME-driven shock at 0.40 and 0.96 au. (a) The magnetic field magnitude measured by *MESSENGER* between 10:00 UT and 16:00 UT on 2013 November 30. (b)–(e) The magnetic field magnitude, the proton density, the proton bulk speed, and electric field fluctuations recorded by *STEREO*-A between 17:00 UT and midnight on 2013 December 1.

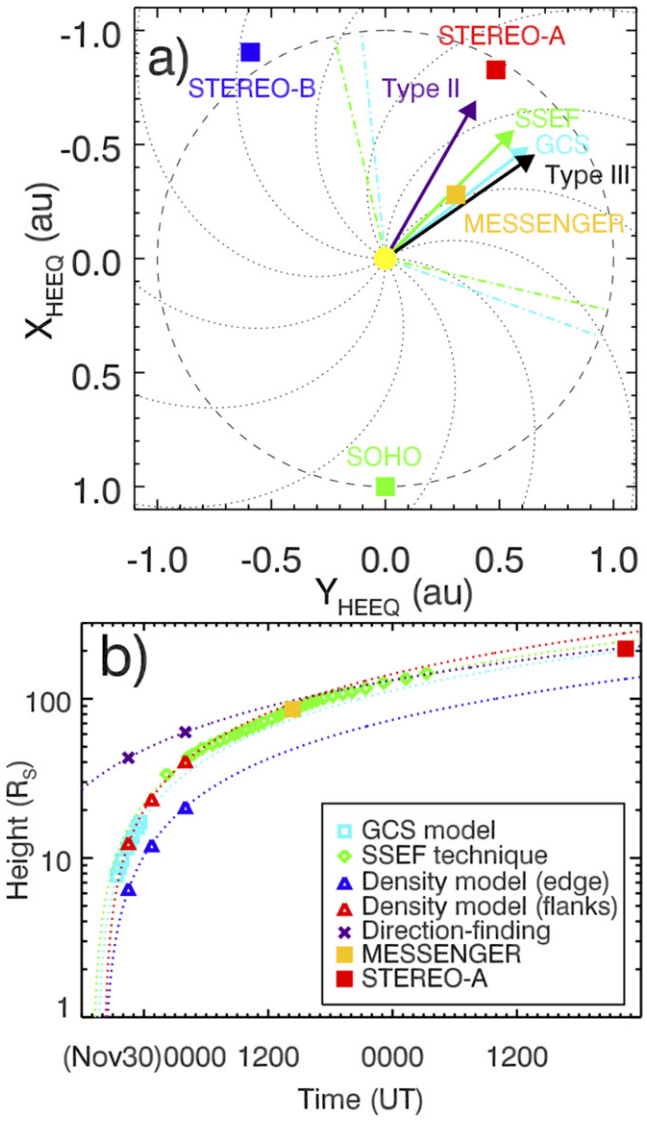

Figure 5. (a) Positions of the spacecraft in the solar equatorial plane on 2013 November 29. The purple and arrows indicate average directions of type II and type III bursts, respectively. The cyan and green arrows indicate the CME propagation directions obtained by the GCS model and the SSEF technique, respectively. Dotted–dashed lines show the CME half-width. (b) Kinematics of the CME and radio sources between 2013 November 29 and December 1. Dotted lines are linear fits.

from which we derive their propagation directions. Results for the propagation direction obtained for the type III burst are in a very good agreement with the results of GCS and SSEF fitting (Figure 5(a)). This suggests that in some cases type III bursts could be useful for estimating CME directions although they are related to solar flares instead of CMEs; a more statistical approach is required to confirm whether this is the case generally. Moreover, intense interplanetary type III bursts are more frequently observed than interplanetary type II bursts (Gopalswamy 2011). In contrast, the locations of the type II bursts seem to lie at the CME flanks. Hence, they are consistent with the CME-driven shock rather than the driver itself. We note that the type III burst may not be related to this eruption since it occurred five hours after the CME liftoff. However, it was the first complex type III burst observed since then, and we thus performed the radio triangulation for a comparison with the CME kinematics. Nonetheless, type II bursts occur sometimes without any type III bursts around.

Figure 5(b) displays kinematics of the CME leading edge and radio sources. The results from the various techniques are in good agreement with the CME-driven shock arrival times at *MESSENGER* and *STEREO-A*. For an analysis of the type II frequency drift, we converted frequencies of the type II burst f to radial distances r using the density model of Sittler & Guhathakurta (1999). As in Figure 2, we consider two possible scenarios: the emission originates at the CME leading edge ($r \sim f$) and flanks ($r/\cos\lambda_{GCS} \sim f$). A comparison with white-light and in situ measurements suggests that the latter is valid, and the derived average speed of the CME-driven shock from a frequency drift is then $992 \pm 22\,\mathrm{km\,s^{-1}}$, which is consistent with an assumption that the CME-driven shock propagates faster than the CME itself. For further analysis of the type II burst, we use a relation between the drift rate df/dt of radio emissions measured at the frequency f, and the radial source speed v:

$$\frac{df}{dt} = \frac{fv}{2n}\frac{dn}{dr}, \quad (1)$$

where n is the density and r is the radial distance (Mann et al. 1999). If we assume that below 1 MHz the CME-driven shock is far enough that $n \sim r^{-2}$, we can calculate ξ the angular deviation of the type II burst propagation direction from radial

by combining radio measurements with white-light observations as

$$\xi = \cos^{-1}\left(\frac{f v_{\rm WL}}{\frac{df}{dt} r_{\rm WL}}\right), \quad (2)$$

where $r_{\rm WL}$ and $v_{\rm WL}$ are the radial distance and the speed of the CME from white-light observations, respectively. From radio and white-light parameters between the first and the second interval ($f = 1.05$ MHz, $v_{\rm WL(GCS)} = 761\,{\rm km\,s^{-1}}$, $df/dt = 116\,{\rm Hz\,s^{-1}}$, and $r_{\rm WL(GCS)} = 16\ R_{\rm S}$), we calculate ξ to be 52°, whereas for parameters between the second and the third interval yield $\xi = 62°$ ($f = 450$ kHz, $v_{\rm WL(SSEF)} = 862\,{\rm km\,s^{-1}}$, $df/dt = 37\,{\rm Hz\,s^{-1}}$, and $r_{\rm WL(SSEF)} = 32\ R_{\rm S}$). Our results confirm that the type II burst arises from the CME flanks since the calculated values of ξ are comparable to the CME angular half-width $\lambda_{\rm GCS}$.

3. CONCLUSIONS

The CME that was launched from the Sun at around 16:00 UT on 2013 November 29 was well imaged by three widely separated coronagraphs on board the *STEREO-A*, *STEREO-B*, and *SOHO* spacecraft (Figure 1). We were thus able to apply the GCS model to perform 3D reconstruction of the CME between 7 $R_{\rm S}$ and 16 $R_{\rm S}$. We also applied the SSEF technique to the time-elongation profile of the CME apex extracted from *STEREO-A*/SECCHI/HI, which allows us to track the CME from 30 $R_{\rm S}$ to 140 $R_{\rm S}$. We find that the speeds and directions derived from GCS and SSEF are comparable. Furthermore, the CME-driven interplanetary shock was subsequently observed in situ at *MESSENGER* and *STEREO-A*, at 0.4 au and 1 au from the Sun, respectively. The GCS and SSEF analysis can be used to make a reasonable prediction of the arrival time of the CME-driven shock at *MESSENGER* and *STEREO-A*.

We have also performed an analysis of the type II and type III bursts associated with this event (Figure 2). We have successfully applied triangulation analysis to the three intervals of the type II burst and the single type III burst (Figure 3). The relative positions of the first interval of the triangulated type II burst suggest that this emission is probably generated by an interaction between the CME-driven shock and the two streamers (Figure 1(c)). The averaged directions, from triangulation, of the type III burst coincide radio sources with the CME direction from GCS and SSEF fitting, while the directions of the type II burst indicate that their source regions are related to interaction of the CME-driven shock with the two streamers.

This CME would possibly trigger a geomagnetic storm if Earth directed and lead to southward magnetic field at 1 au. We thus conclude that interplanetary radio emissions can provide us with an additional tool for predicting both CME-driven shock speed (using a frequency drift) and direction (obtained by radio triangulation) with potential applications in space weather forecasting. Currently, there are only two spacecraft in operation that carry coronagraphs (*SOHO* and *STEREO-A*) and our ability to obtain reliable estimates of the time of arrival of CMEs and their shocks would be significantly curtailed if any one of them failed. We believe that the monitoring of CME-driven shocks, from both a scientific and space weather perspective, would be enriched by the addition of space-borne radio instrumentation. From our perspective, this would be best served by the monitoring interplanetary emissions from at least two vantage points, preferably at L_1 and L_5.

The presented work has been supported by the European Union Seventh Framework Programme (FP7/2007–2013) under grant agreement No. 606692 [HELCATS] and by the Praemium Academiae award of The Czech Academy of Sciences. O.K. and J.S. thanks the support of the Czech Science Foundation grants GP16-16050Y and GAP209/12/2394, respectively. O.S. acknowledges additional support from the LH15304 grant. A.V. was supported by NASA contract S-136361-Y to NRL. V.B. acknowledges support of the CGAUSS (Coronagraphic German And US Solar Probe Plus Survey) project for WISPR by the German Space Agency DLR under grant 50 OL 1201.

REFERENCES

Bale, S. D., Ullrich, R., Goetz, K., et al. 2008, SSRv, 136, 529
Bougeret, J. L., Goetz, K., Kaiser, M. L., et al. 2008, SSRv, 136, 487
Bougeret, J.-L., Kaiser, M.-L., Kellogg, P. J., et al. 1995, SSRv, 71, 231
Cairns, I. H., Knock, S. A., Robinson, P. A., & Kuncic, Z. 2003, SSRv, 107, 27
Cecconi, B., Bonnin, X., Hoang, S., et al. 2008, SSRv, 136, 549
Cremades, H., Cyr, O. C., St., & Kaiser, M. L. 2007, SpWea, 5, S08001
Davies, J. A., Harrison, R. A., Perry, C. H., et al. 2012, ApJ, 750, 23
Domingo, V., Fleck, B., & Poland, A. I. 1995, SoPh, 162, 1
Gary, D. E., Dulk, G. A., House, L., et al. 1984, A&A, 134, 222
Ginzburg, V. L., & Zhelezniakov, V. V. 1958, SvA, 2, 653
Gopalswamy, N. 2011, in Planetary, Solar and Heliospheric Radio Emissions, held at Graz, Austria, September 15–17, 2010, 325
Gopalswamy, N., Aguilar-Rodriguez, E., Yashiro, S., et al. 2005, JGRA, 110, A12S07
Gopalswamy, N., Davila, J. M., Auchére, F., et al. 2011b, Proc. SPIE, 8148, 81480Z
Gopalswamy, N., Davila, J. M., St. Cyr, O. C., et al. 2011a, JASTP, 73, 658
Gopalswamy, N., Lara, A., Lepping, R. P., et al. 2000, GeoRL, 27, 145
Gopalswamy, N., Mäkelä, P., Akiyama, S., et al. 2015, ApJ, 806, 8
Gopalswamy, N., Yashiro, S., Kaiser, M. L., Howard, R. A., & Bougeret, J.-L. 2001, ApJL, 548, L91
Graham, D. B., & Cairns, I. H. 2015, JGRA, 120, 4126
Howard, R. A., Moses, J. D., Vourlidas, A., et al. 2008, SSRv, 136, 67
Kaiser, M. L., Reiner, M. J., Gopalswamy, N., et al. 1998, GeoRL, 25, 2501
Krupar, V., Kontar, E. P., Soucek, J., et al. 2015, A&A, 580, A137
Krupar, V., Maksimovic, M., Santolik, O., et al. 2010, in AIP Conf. Ser. 1216, The Apparent Source Size of Type III Radio Bursts: Preliminary Results by the STEREO/WAVES Instruments, ed. M. Maksimovic et al. (Melville, NY: AIP), 284
Krupar, V., Maksimovic, M., Santolik, O., Cecconi, B., & Kruparova, O. 2014a, SoPh, 289, 4633
Krupar, V., Maksimovic, M., Santolik, O., et al. 2014b, SoPh, 289, 3121
Krupar, V., Santolik, O., Cecconi, B., et al. 2012, JGR, 117, A06101
Magdalenić, J., Marqué, C., Krupar, V., et al. 2014, ApJ, 791, 115
Mann, G., Jansen, F., MacDowall, R. J., Kaiser, M. L., & Stone, R. G. 1999, A&A, 348, 614
Martínez Oliveros, J. C., Lindsey, C., Bale, S. D., & Krucker, S. 2012a, SoPh, 279, 153
Martínez Oliveros, J. C., Raftery, C. L., Bain, H. M., et al. 2012b, ApJ, 748, 66
Martínez-Oliveros, J. C., Raftery, C., Bain, H., et al. 2015, SoPh, 290, 891
Melrose, D. B. 1980, SSRv, 26, 3
Reiner, M. J., Goetz, K., Fainberg, J., et al. 2009, SoPh, 259, 255
Reiner, M. J., Kaiser, M. L., Fainberg, J., Bougeret, J.-L., & Stone, R. G. 1998a, GeoRL, 25, 2493
Reiner, M. J., Kaiser, M. L., Fainberg, J., & Stone, R. G. 1998b, JGR, 103, 29651
Reiner, M. J., Kaiser, M. L., Karlický, M., Jiřička, K., & Bougeret, J.-L. 2001, SoPh, 204, 121
Reiner, M. J., Vourlidas, A., Cyr, O. C. S., et al. 2003, ApJ, 590, 533
Santolík, O., Parrot, M., & Lefeuvre, F. 2003, RaSc, 38, 010000
Schmidt, J. M., & Cairns, I. H. 2016, GeoRL, 43, 50
Sittler, E. C., Jr., & Guhathakurta, M. 1999, ApJ, 523, 812

Solomon, S. C., McNutt, R. L., Gold, R. E., & Domingue, D. L. 2007, SSRv, 131, 3
Steinberg, J. L., Hoang, S., & Dulk, G. A. 1985, A&A, 150, 205
Steinberg, J. L., Hoang, S., Lecacheux, A., Aubier, M. G., & Dulk, G. A. 1984, A&A, 140, 39
Thejappa, G., & MacDowall, R. J. 2010, ApJ, 720, 1395
Thejappa, G., MacDowall, R. J., & Kaiser, M. L. 2007, ApJ, 671, 894
Thernisien, A., Vourlidas, A., & Howard, R. A. 2009, SoPh, 256, 111
Vourlidas, A. 2004, in Radio Observations of Coronal Mass Ejection, Vol. 314, ed. D. E. Gary, & C. U. Keller (Dordrecht: Springer), 223
Vourlidas, A. 2015, SpWea, 13, 197
Wild, J. P. 1950, AuSRA, 3, 541
Wild, J. P., & McCready, L. L. 1950, AuSRA, 3, 387
Xie, H., Odstrcil, D., Mays, L., et al. 2012, JGR, 117, A04105